Geophys. J. Int. (1999) **137,** 51–63

The thin hot plume beneath Iceland

Richard M. Allen,[1] Guust Nolet,[1] W. Jason Morgan,[1] Kristín Vogfjörd,[1]
Bergur H. Bergsson,[2] Pálmi Erlendsson,[2] G. R. Foulger,[3] Steinunn Jakobsdóttir,[2]
Bruce R. Julian,[4] Matt Pritchard,[3] Sturla Ragnarsson[2] and Ragnar Stefánsson[2]

[1] *Department of Geosciences, Guyot Hall, Princeton University, Princeton,* NJ 08544, *USA. E-mail: rallen@geo.princeton.edu*
[2] *Veðurstofa Íslands, Bústaðavegur* 9, 150 *Reykjavik, Iceland*
[3] *Department of Geological Sciences, University of Durham, South Road, Durham,* DH1 3LE, *UK*
[4] *US Geological Survey,* 345 *Middlefield Rd,* MS 977, *Menlo Park,* CA 94025, *USA*

Accepted 1998 October 6. Received 1998 October 2; in original form 1998 May 18

SUMMARY

We present the results of a seismological investigation of the frequency-dependent amplitude variations across Iceland using data from the HOTSPOT array currently deployed there. The array is composed of 30 broad-band PASSCAL instruments. We use the parameter t^*, defined in the usual manner from spectral ratios (Halderman & Davis 1991), to compare observed *S*-wave amplitude variations with those predicted due to both anelastic attenuation and diffraction effects. Four teleseismic events at a range of azimuths are used to measure t^*. A 2-D vertical cylindrical plume model with a Gaussian-shaped velocity anomaly is used to model the variations. That part of t^* caused by attenuation was estimated by tracing a ray through IASP91, then superimposing our plume model velocity anomaly and calculating the path integral of $1/vQ$. That part of t^* caused by diffraction was estimated using a 2-D finite difference code to generate synthetic seismograms. The same spectral ratio technique used for the data was then used to extract a predicted t^*. The t^* variations caused by anelastic attenuation are unable to account for the variations we observe, but those caused by diffraction do. We calculate the t^* variations caused by diffraction for different plume models and obtain our best-fit plume, which exhibits good agreement between the observed and measured t^*. The best-fit plume model has a maximum *S*-velocity anomaly of -12 per cent and falls to 1/e of its maximum at 100 km from the plume centre. This is narrower than previous estimates from seismic tomography, which are broadened and damped by the methods of tomography. This velocity model would suggest greater ray theoretical traveltime delays than observed. However, we find that for such a plume, wave-front healing effects at frequencies of 0.03–0.175 Hz (the frequency range used to pick *S*-wave arrivals) causes a 40 per cent reduction in traveltime delay, reducing the ray theoretical delay to that observed.

Key words: attenuation, diffraction, plume, *S* waves, spectral analysis, upper mantle.

1 INTRODUCTION

The Iceland hotspot, located on the mid-Atlantic ridge, has been the subject of many studies aimed at furthering our understanding of mantle convection and plate tectonics. While many of these studies suggest the presence of a mantle plume beneath, some authors dispute the evidence, suggesting that hotspots are the result of anomalous material present only in the uppermost mantle.

Wilson (1963) first hypothesized that there are upwelling regions in the mantle. Morgan (1971) linked surface hotspots with upwelling plumes carrying hot material from the core to the surface—ocean island chains are the result of tectonic plates moving over the top of plumes. Since then various workers have developed numerical models of mantle convection using surface observables such as bathymetry, gravity and heat flow over hotspots as constraints (e.g. McKenzie *et al.* 1974; Courtney & White 1986; Davies 1989; Houseman 1990;

Olsen 1990; Sleep 1990; Watson & McKenzie 1991; Ribe *et al.* 1995). Many of these models provide quantitative predictions of the plume flux; however, there is usually a trade-off between plume diameter and temperature anomaly which is not well constrained.

An alternative approach of obtaining information about plume structure is seismic tomography. Tryggvasson *et al.* (1983) conducted the first such study in Iceland and found a vertical region of low velocity in the depth range 0–400 km. More recently, Wolfe *et al.* (1997) published a tomographic image which showed a more continuous low-velocity region extending from 100 km down to 400 km with a vertically cylindrical geometry.

In this paper we present evidence not only for the existence of a plume beneath Iceland, but also for its radius by studying the diffraction effects of the plume on seismic energy passing through it. We consider amplitude variations of shear-wave arrivals in Iceland as a function of frequency and position. To do this we use the parameter t^*, which in the past has primarily been used to study anelastic attenuation, Q (e.g. Lees & Lindley 1994; Slack *et al.* 1996). In the case of Iceland, however, we find diffraction to be the dominant control on amplitude variations as observed using the parameter t^*, not anelastic attenuation. We model these effects using a finite difference code and compare the results to those observed for several events recorded on the HOTSPOT array across Iceland. This technique provides an alternative method to seismic tomography for measuring the size of the plume in terms of its diameter and velocity anomaly.

We note the recent paper by Tilmann *et al.* (1998), published since this paper was reviewed. In it they conduct a theoretical study of scattering from a vertical cylinder of low-velocity material. Their predicted amplitudes are very similar to those we present here.

2 t^*

The parameter t^* (with units of seconds) was originally defined in terms of anelastic attenuation, Q, where

$$t^* = \int_{\text{path}} \frac{dx}{vQ} \tag{1}$$

and

$$A = A_0 \, \mathrm{e}^{-\pi t^* f} \, . \tag{2}$$

f is frequency and v is seismic velocity. The quantity t^* has been used in many studies as a first step towards obtaining a Q model. First t^* is obtained from the data, then normal tomographic inversion techniques may be used to calculate a 3-D Q model for the subsurface beneath the station array, given a velocity model. Several methods of obtaining t^* are available, depending on whether the data sources are local (Lees & Lindley 1994; Wu & Lees 1996), regional (Myers, personal communication, 1996) or teleseismic (Taylor *et al.* 1986; Halderman & Davis 1991; Slack *et al.* 1996; Bhattacharyya *et al.* 1996). The method we use is most similar to that of Halderman & Davis (1991), and uses a spectral ratio technique.

It is commonly assumed that attenuation is the dominant cause of amplitude variations, and an accepted method for measuring this t^* is as follows: The data are first time-windowed around the shear-wave phase of interest and the Fourier transform calculated. To calculate the spectral ratios the amplitude spectrum of one station is divided by that of another, which removes the source signal and common path effects, leaving instrument effects and anelastic attenuation differences:

$$\frac{A_i(f)}{A_j(f)} = \frac{G_i(f) \, \mathrm{e}^{-\pi t_i^* f}}{G_j(f) \, \mathrm{e}^{-\pi t_j^* f}} \, , \tag{3}$$

where the indices i and j represent different stations, A is the amplitude spectrum, G represents the instrument effects and f is the frequency. We take the natural logarithm to obtain

$$\ln \frac{A_i}{A_j} = \ln \frac{G_i}{G_j} - \pi f (t_i^* - t_j^*) \, . \tag{4}$$

The difference $t_i^* - t_j^*$ (or δt_{ij}^*) is calculated for all pairs of stations by fitting the best-fit straight line to $\ln(A_i/A_j)$ versus frequency.

Apart from an unknown baseline, individual t^* values can be computed from these differences. As we shall show, attenuation is not the dominant control on these 't^*' variations in Iceland, so to avoid confusion we use the symbol s^* for our *measured* value of 't^*' from the data. We continue to use the symbol t^* when referring to the 't^*' variations due to attenuation, but we use d^* for variations due to diffraction effects.

Diffraction effects probably have an effect on amplitude which varies with frequency in a more complicated manner than (2), depending on the shape of the diffracting anomaly. However, experience shows that amplitude spectra or their ratios often have a large variance and any modelling more sophisticated than a linear fit to $\ln(A_i/A_j)$ is unwarranted. This implies that our measured value s^* is due to the sum of attenuation (t^*) and diffraction (d^*) effects:

$$s^* = t^* + d^* \, . \tag{5}$$

Although we do apply the same measurement technique to the data in our study, we refrain from a simplified interpretation in terms of attenuation t^* only. No adequate inversion method is available to model the diffraction effects we observe. Rather, we shall try to model our observations of s^* by comparing them with direct finite difference calculations of the diffracting effects (d^*) of simplified plume models, and ray theoretical calculations for the expected effect of attenuation (t^*). We note that t^* observations are in general notoriously noisy, so we shall not try to obtain more than a qualitative fit.

As defined above, anelastic attenuation has a very simple effect on t^*: it is the path integral of $1/vQ$. High attenuation (low Q) results in a high value of t^*. We expect the high-temperature plume beneath Iceland to be more highly attenuating than the mantle material around. This would be observed in the data as high positive values at stations where the ray has travelled through the most plume material, and negative values at stations which do not sample the plume (the negative values are due to the subtraction of the mean t^* value). In terms of the gradient of the amplitude spectrum, the plume attenuates the high frequencies resulting in a reduced gradient or positive t^* value.

Diffraction of rays due to velocity variations is more complex than anelastic attenuation. A low-velocity cylindrical plume acts like a lens: rays refract around it causing focusing.

The focusing is frequency-dependent, however. If high frequencies are focused more strongly than low frequencies—an effect we would expect in the wake of the plume—we should observe low or negative values of d^*. Conversely, in the shadow zones where low frequencies can penetrate more easily, high values of d^* are expected.

3 DATA

3.1 The network

The data used in this study come from the HOTSPOT network (Fig. 1), a PASSCAL array deployed across Iceland from summer 1996. The network consists of 30 broad-band instruments deployed to complement the SIL network, giving good coverage everywhere on the island. The SIL network is a permanent network operated by Vedurstofa Islands consisting of approximately 30 stations with broad-band or short-period sensors. Five of the SIL locations were temporarily provided with a PASSCAL broad-band sensor. The SIL stations are concentrated in the southwest and north of Iceland where seismic activity and population are higher. The HOTSPOT instruments cover the rest of Iceland with a typical station spacing of 50 km.

The PASSCAL instruments are mainly Guralp CMG3-ESPs, although there are four Guralp CMG-40Ts and one Guralp CMG-3T. The instruments are connected to DAS digitizers recording at 20 samples per second. The data are stored on field disks which are changed every 1–4 months. A GPS clock operates at each station. The HOTSPOT network remained in Iceland until August 1998.

The PASSCAL instruments are at temporary sites. Data quality compares well with a borehole instrument located in Iceland (Global Seismic Network station BORG). Fig. 2 shows a comparison plot of four broad-band waveforms

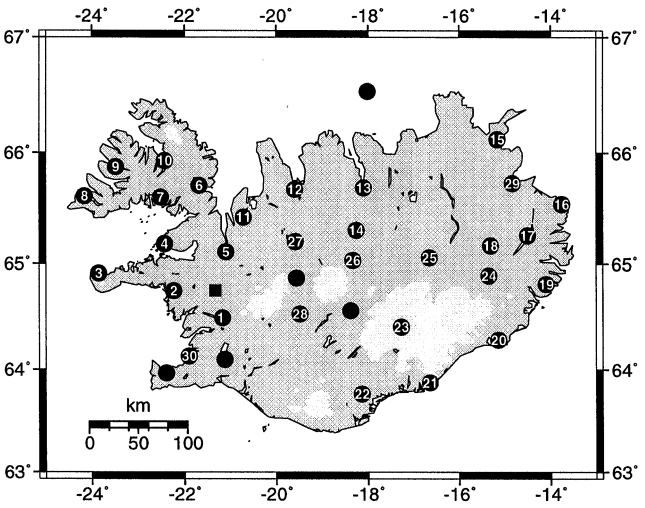

Figure 1. Map showing the locations of the 35 PASSCAL stations. The numbered dots show the HOTSPOT network, consisting of 30 stations. The remaining dots represent the PASSCAL instruments operating as part of the SIL network. The apparent gaps to the north and southwest are filled by the permanent SIL network, not shown here. The square is BORG, part of the Global Seismic Network. Typical station spacing is 50 km.

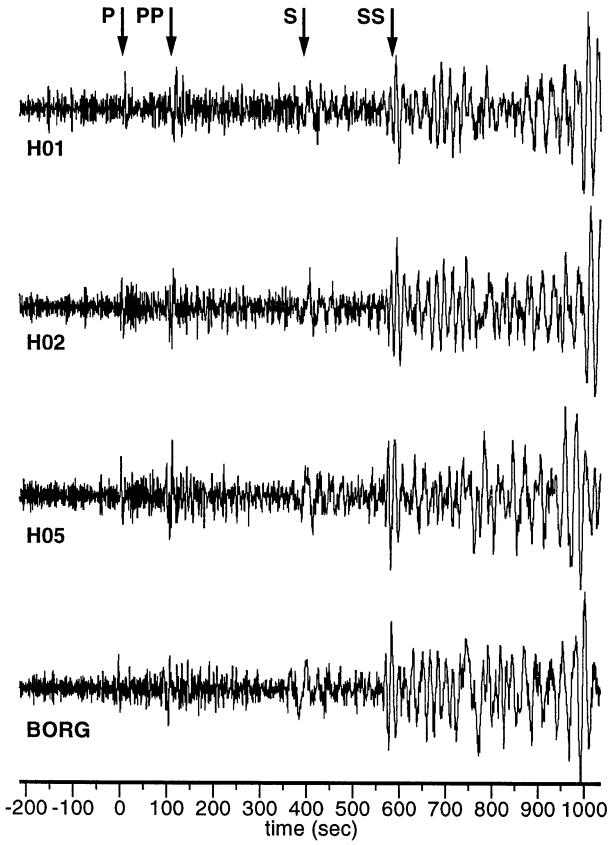

Figure 2. Example of the data quality from the temporary HOTSPOT network compared to BORG, a borehole instrument which is part of the Global Seismic Network. The broad-band record is from the 1996 July 20 event in the Aegean. The four stations are all located in a cluster in western Iceland. See Fig. 1 for locations.

recorded for the same teleseismic event. The data are from BORG and H01, H02 and H05, the three HOTSPOT stations surrounding BORG (Fig. 1). The signal-to-noise ratio is similar at the temporary and the borehole stations. The poor signal-to-noise ratio is due to the high microseismic noise level. Comparisons of the amplitude spectra are available at http://geo.princeton.edu/~rallen/research/HOTvsBORG.

3.2 Microseismic noise

Microseismic noise is high on all instruments in Iceland as no point is far from the Atlantic Ocean. Fig. 3 shows a typical spectrum. It is from a vertical-component recording lasting 1200 s without any seismic arrivals. The single microseismic noise peak is consistently at 0.25 Hz and noise levels are significant between 0.2 and 0.8 Hz. This noise peak dominates any signal within this frequency range with the exception of magnitude $\sim$ 4 or greater local events.

3.3 Measurement of s^*

As described above we use a spectral ratio technique to obtain s^* from the shear-wave arrivals. The data are first time-windowed around the phase of interest. The window length is chosen for each event to optimize the signal-to-noise ratio. Time-window lengths varied between 50 and 80 s. Fig. 4(a)

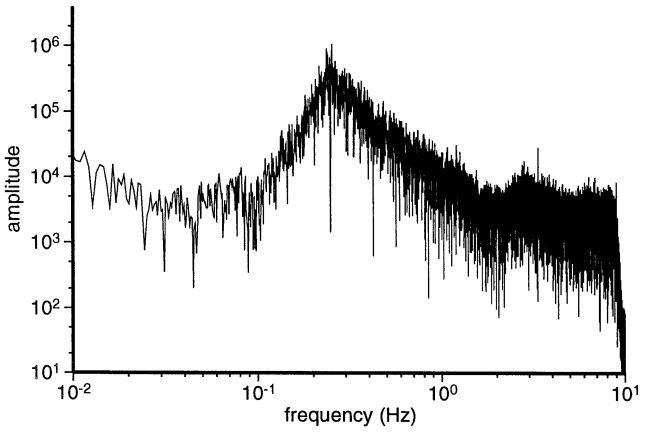

Figure 3. Amplitude spectrum calculated from 1200 s of noise from HOTSPOT station 13. There were no earthquake arrivals during this period. It shows the characteristic microseismic noise peak for Iceland at 0.25 Hz which dominates all arrivals in this frequency range other than local earthquakes greater than magnitude ~4.

shows waveforms from two stations for the 1996 July 20 Aegean event (Table 1); the *SS* arrival is indicated. The Fourier transform is calculated, both for the *S* arrival and a time window of equal length just before the arrival, as an indicator of the noise levels. Figs 4(b) and (c) show the amplitude spectra of the signal and noise windows for the seismograms in Fig. 4(a). Such plots allow the selection of frequency windows where the signal-to-noise ratios are good. We only used frequencies where the signal-to-noise ratio was greater than 5. A typical useful range was 0.03–0.175 Hz. This frequency window is below the microseismic noise peak and extends down to the natural frequency of the instrument. The amplitude spectrum of one station is divided by that of another to obtain the spectral ratio (Fig. 4d), and the best-fit gradient calculated. We do this for all unique pairs of stations.

Fig. 5 illustrates the variation in closeness of fit of the linear approximation to the spectral ratios. The best-fit line was obtained by minimizing the sum of the absolute misfits. For each of the δs_{ij}^* fits we obtain a mean absolute deviation as an estimate of the goodness of fit. Fig. 5(a) is a histogram of the mean absolute deviation values for the 785 δs_{ij}^* fits from the four teleseismic events (Table 1). As an example of the goodness of fit, Figs 5(b) and (c) show the spectral ratios for different pairs of stations from the 1996 November 12 Peru event and the 1996 November 19 Kashmir event, respectively. The best-fit line is also shown. The mean absolute deviations of the points from the best-fit lines are 0.280 and 0.489 for Figs 5(b) and (c), respectively. 50 per cent of the δs_{ij}^* measurements have a smaller mean absolute deviation than Fig. 5(b). 90 per cent are better than Fig. 5(c).

The values of s^* are obtained from all δs_{ij}^* by least squares, in a similar way to that used by Van Decar & Crosson (1990) to calculate relative traveltimes. Once the additional constraint that the sum of s^* equals zero for each event is added, the relative values of s^* take the form

$$s_i^* = -\sum_{j \neq i} \delta s_{ij}^*, \tag{6}$$

where i is the index of the station for which s^* is being calculated and j is that of the other stations.

We present in this paper the s^* measurements from four teleseismic events that occurred in the first six months of the HOTSPOT deployment. They are at a range of azimuths, perpendicular and oblique to the Neovolcanic Zones (representing the mid-Atlantic ridge through Iceland). We use the *S* or *SS* arrival, depending on which has the higher signal-to-noise ratio. The event parameters are shown in Table 1.

4 MODELLING FREQUENCY-DEPENDENT AMPLITUDE VARIATIONS

4.1 Modelling the plume

We wish to estimate the effects of both anelastic attenuation and diffraction on the measured value of s^*. To do this we use a simple 2-D vertically cylindrical plume model with a Gaussian-shaped velocity perturbation, δv, from some background earth velocity model,

$$\delta v = \delta v_{\max} \, \mathrm{e}^{-\left(\frac{x^2}{l^2}\right)}, \tag{7}$$

where $\delta v_{\max}$ is the maximum *S*-velocity perturbation at the centre of the plume, x is the radial distance from the plume centre and l is the Gaussian width. We vary the size and velocity anomaly of the plume using l and $\delta v_{\max}$, respectively. This 2-D cylindrical plume is a first approximation to true plume structure. It does not include any non-radially symmetric features such as the mid-Atlantic ridge. Our data do not show much variation with azimuth, suggesting that a radially symmetric model is adequate.

We will refrain here from referring to a plume radius or diameter as this requires an arbitrary choice of how much the velocity perturbation must have decayed towards the background. Instead, we will refer to l, the radius at which the velocity anomaly is 1/e of the maximum, which is what some authors refer to as the radius.

The use of a Gaussian-shaped plume model is based on theoretical calculations of plume flow (Loper & Stacey 1983) and is used in most calculations (e.g. Ribe *et al.* 1995; Ito *et al.* 1996). A Gaussian variation also conforms to observations. Fig. 6 shows data points (squares) from Wolfe *et al.* (1997) and the best-fit Gaussian curve to their data, which provides an excellent fit. The data points were measured from the 2-D

Table 1. Event parameters and phases used for the four events. The epicentral distance is to the centre of Iceland.

Date	Time	Lat.	Long.	Ms	Backazimuth	Δ	Phase	Region
20 Jul 96	00 : 00 : 42.7	36.3049°N	27.0194°E	6.2	116°	38.6°	*SS*	Aegean
9 Oct 96	13 : 10 : 52.0	34.4923°N	32.1185°E	6.8	110°	42.1°	*S*	Cyprus
12 Nov 96	16 : 59 : 43.4	14.8955°S	75.4865°W	7.3	−125°	88.7°	*S*	Peru
19 Nov 96	10 : 44 : 45.1	35.2285°N	78.2498°E	7.1	68°	59.9°	*S*	Kashmir

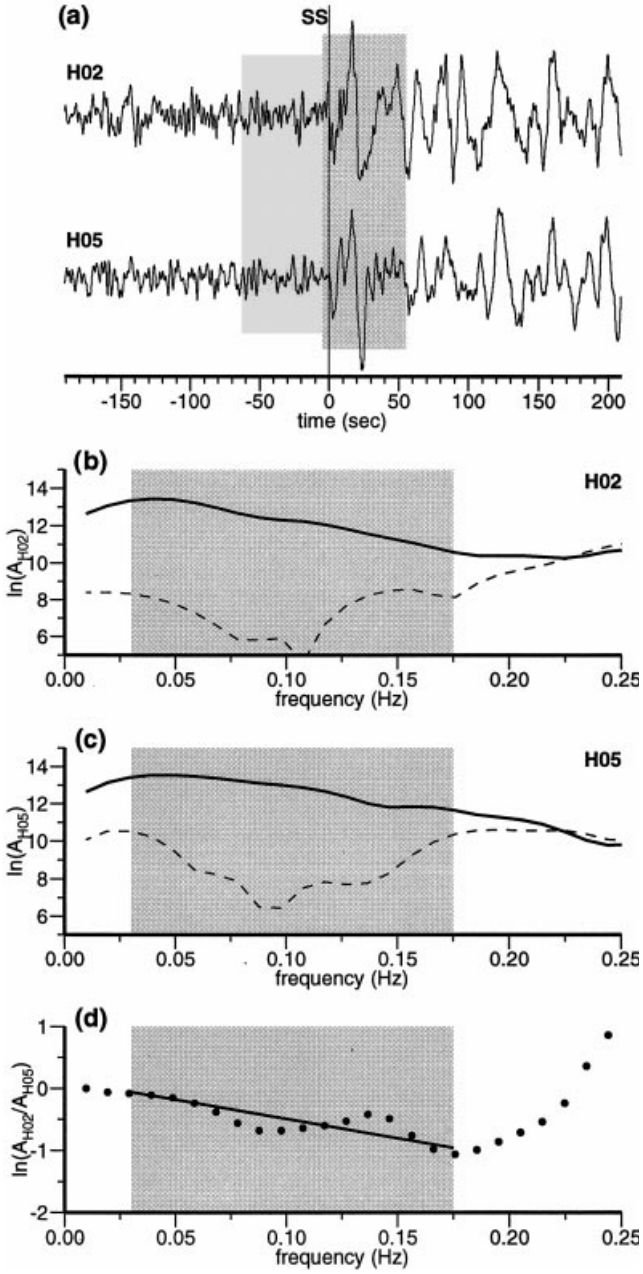

Figure 4. (a) Broad-band waveforms from HOTSPOT stations H02 and H05 for the 1996 July 20 Aegean event. The *SS* arrivals have been aligned as indicated by the vertical bar. The time window used in this case was 60 s as indicated by the darker grey box. A window of equal length prior to the arrival was used to calculate the noise spectra as shown by the light grey box. (b) Amplitude spectra for H02: the solid line shows that of the signal time window, the dashed, the noise time window. The vertical scale shows the natural logarithm of the amplitude. The shaded box represents the frequency window used to calculate the spectral ratio. At lower frequencies we approach the natural frequency of the instrument, at higher, we enter the micro-seismic noise band. (c) Amplitude spectra for H05. (d) Spectral ratio for stations H02 and H05. The dots represent the data. The line is the best-fit linear trend to the data within the useful frequency window.

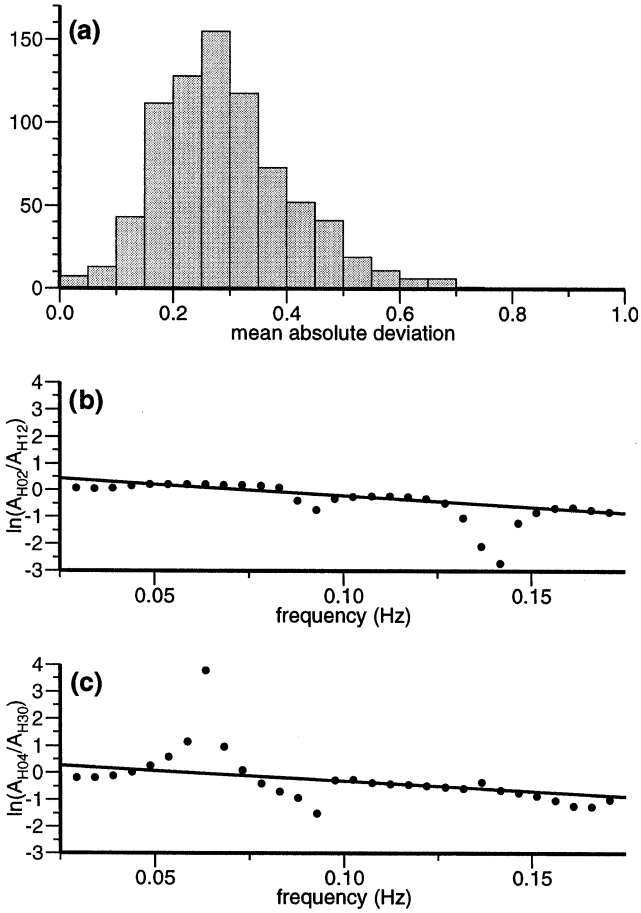

Figure 5. Closeness of fit of the linear approximation to the spectral ratios. (a) Histogram of the mean absolute deviation of data points from the best-fit line for the 785 δs_{ij}^*. (b) Spectral ratio between stations H02 and H12 for the November 12 Peru event. The mean absolute deviation from the best-fit line is 0.280. The mean absolute deviation for 50 per cent of all the δs_{ij}^* are better than this. (c) Spectral ration for H04 and H30 from the 1996 November 19 Kashmir event. The mean absolute deviation is 0.489; 90 per cent of all the δs_{ij}^* are better than this.

section published in Wolfe *et al.* (1997). They were measured at a depth of 300 km, which provides an average radius for the plume velocity model of Wolfe *et al.* (1997), and is also typical for the depth at which rays used in this study pass through the plume beneath Iceland. The data are percentage deviations of the shear-wave velocity model from their background velocity model. The best-fit Gaussian curve through the data has an l of 175 km and a $\delta v_{\max}$ of -4.2 per cent. We shall refer to this model as Plume1.

4.2 t^*—anelastic attenuation

To study the effect of anelastic attenuation on t^* we use a ray theoretical approach. We trace a ray through the IASP91 earth model from a receiver on the surface down to the turning point. We stop at the turning point as we are only interested in relative variations between rays sampling different portions of the plume. The distance of the turning point from the plume is sufficiently large that the plume has no effect beyond this distance. We use this ray path and trace it through our Gaussian plume computing the path integral of dx/vQ. Velocity is determined as a perturbation from IASP91 and Q is obtained from the velocity. This is achieved by combining two of the relationships from Nataf & Ricard (1996). They use the

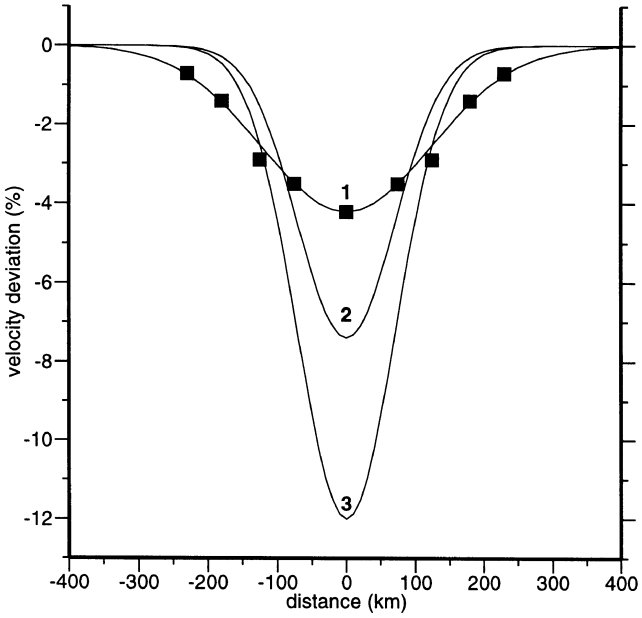

Figure 6. Plot of Gaussian plume models in percentage velocity perturbation. The squares represent the values from Wolfe *et al.* (1997). The perturbations were measured at 300 km depth. The line through them is the best-fit Gaussian which has $dv_{\max} = -4.2$ per cent and $l = 175$ km; we refer to this model as Plume1. The other two lines represent the other plume models, Plume2 and Plume3. The Gaussian which forms Plume2 ($dv_{\max} = -7.4$ per cent and $l = 100$ km) has the same integral as Plume1, which corresponds to near-preserved traveltime delays. Plume3 is our best-fit model ($dv_{\max} = 12$ per cent and $l = 100$ km); it does not preserve traveltime delays but wave-front healing compensates for this.

following constitutive law:

$$X(T, z) = [X_0 + zX_z][1 + X_T(T - T_{\text{ref}})], \tag{8}$$

where X represents density, P- or S-velocity or the natural logarithm of attenuation. By substituting the S-wave velocity and the attenuation versions of this equation into one another we remove the temperature dependence and obtain a relationship for attenuation in terms of S-velocity and depth:

$$\ln Q(\beta, z) = [\ln Q_0 + z \ln Q_z]\left[1 + \frac{\ln Q_T}{\beta_T}\left(\frac{\beta}{\beta_0 + z\beta_z} - 1\right)\right], \tag{9}$$

where Q is the anelastic attenuation at depth z and the shear-wave velocity is β. This approximation was experimentally justified by Lebedev & Nolet (1997). For this calculation we used values of the constants Q_0, Q_z, Q_T, β_0, β_z and β_T for olivine, which are shown in Table 2.

Table 2. Constants used in anelastic attenuation calculations. All values are for olivine and are taken from Nataf & Ricard (1996).

Constant	Value
$\ln Q_0$	3.1
$\ln Q_z$	5×10^{-3}
$\ln Q_T$	-9×10^{-4}
β_0	4.15
β_z	1.75×10^{-3}
β_T	-1.1×10^{-4}

Using Plume1 we calculate t^* due to anelastic attenuation and compare it to s^* measured from the data. Fig. 7 is a plot of the calculated and observed values of t^* and s^* from the Cyprus event (Table 1). The colourscale shows the calculated values due to rays moving through the plume beneath Iceland; the arrow gives the source azimuth. The mean value of t^* was subtracted from all values, which results in slightly negative values of t^* for rays which sample little of the plume; that is, in the area nearest the event and towards the sides of the plume. The rays arriving furthest from the event have sampled most of the plume and accordingly have the highest values of t^*. The variation in t^* between the zero effect away from the plume and the maximum is a simple monotonic increase as the ray samples more of the plume. Increased anelastic attenuation can only result in increased positive values of t^*. The map of Iceland and observed values of s^* (black numbers) have been rotated so the backazimuth of the event is parallel to the ray propagation direction in the model. The data show both positive and negative values of s^*. However, they have a very different pattern to t^*. The highest negative s^* observation of -2.6 s is very close to the predicted highest and positive t^* value

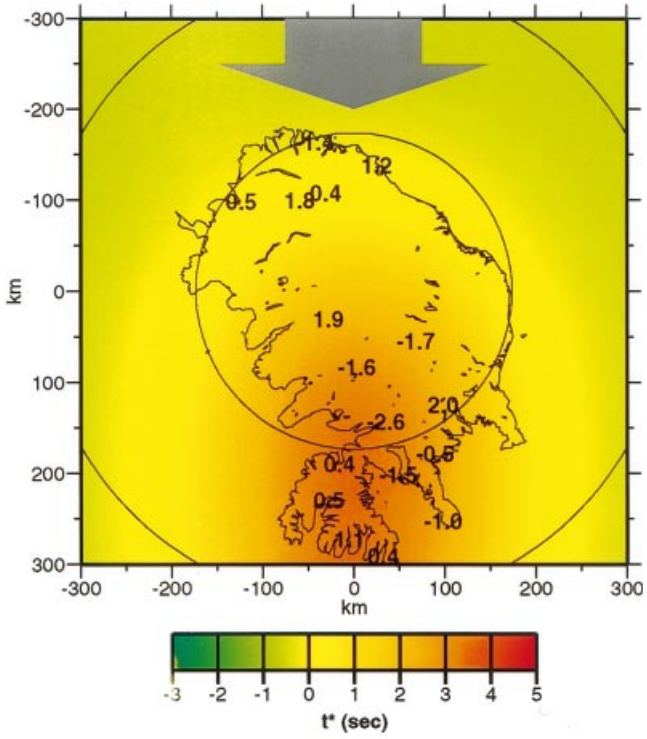

Figure 7. Comparison of the expected variations due to anelastic attenuation (t^*) associated with Plume1 with those observed (s^*) for the Cyprus event. The colourscale shows the predicted variation for an event at the same epicentral distance as the Cyprus event. The arrow indicates the horizontal velocity component of the rays in the model and the two circles represent distances of l and $2l$ from the centre of the plume. The average t^* value is subtracted from all other values, resulting in slightly negative values for rays not sampling the plume and the greatest positive values for those sampling most of the plume. Overlain is a map of Iceland which has been rotated so the back-azimuth of the event is parallel to the direction of ray propagation in the model. The observed s^* have both positive and negative values for rays sampling the plume, in contrast with calculated t^* from the model.

of ~4 s. Clearly, anelastic attenuation cannot explain the magnitude of variations in s^* observed, nor can it model the very strong horizontal gradients in s^*.

4.3 d^*—diffraction and focusing

To study the diffraction effects around the plume we use a 2-D finite difference code (Marquering 1991). We consider the curved path of an incident teleseismic ray (Fig. 8a). The 2-D plane of the finite difference calculation is the plane perpendicular to this path (in and out of the plane of Fig. 8a). When we slice through the plume obliquely, the cylindrical plume appears elliptical as shown in Fig. 8(b). We use a major to minor axis ratio of 2, equivalent to the ray cutting the plume at 30° from the vertical, which is a typical angle for the rays in this study. The two ellipses (Fig. 8b) represent distances l and $2l$ from the centre of the plume, where the velocity perturbation has fallen to e^{-1} and e^{-4}, respectively.

We represent the incoming 3-D plane wave by a line source in this 2-D simulation, located at the bottom of the cross-section shown in Fig. 8(b). The use of a 2-D rather than a 3-D finite difference algorithm involves a small error, since vertical shifts in the wave front cannot be modelled. This error is akin to the linearization error in body-wave tomography, where ray bending is ignored. Lateral differences in the vertical shift may have an effect on the amplitudes but it is reasonable to assume that this is much smaller than the focusing. The latter is correctly modelled since we assume the plume to have cylindrical symmetry. The source used was a Berlage wavelet (Aldridge 1990), its shape chosen to include all frequencies in the useful frequency window of the data, 0.03–0.175 Hz. Its characteristic frequency, based on the rise time of the wavelet, is 0.07 Hz.

The waveforms were recorded throughout the finite difference plane. A horizontal line of waveforms (Fig. 8b) represents recordings at the same epicentral distance; that is, the recordings in a line across Iceland perpendicular to the backazimuth. The seismograms recorded from the top of the plane of Fig. 8(b) represent those recorded on the far side of Iceland from the event. A ray which arrives at the surface in the centre of Iceland has travelled an almost identical path to those arriving on the far side, except it has only travelled through half the plume. As we are using a 2-D plume model, the recorded seismogram at a position halfway through the plume in Fig. 8(b) is equivalent to the signal recorded at a station halfway across Iceland.

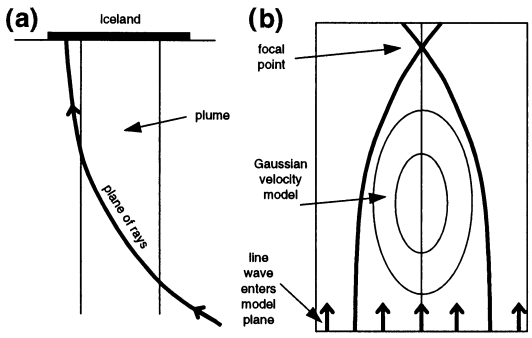

Figure 8. Cartoon showing how the 2-D finite difference calculation was used to model the 3-D plume. (a) Cross-section through the mantle beneath Iceland parallel to the backazimuth of the event. It shows a ray diffracting through the mantle and arriving at a station on the far side of Iceland from the event. (b) The 2-D plane of the finite difference calculation; this is the plane including the ray in (a) and perpendicular to the paper. The two ellipses represent distances of l and $2l$ from the centre of the plume. The line source enters at the bottom of (b) and is focused by the low-velocity plume in the manner shown by the curved bold lines to a focal point.

The synthetic waveforms were used to obtain d^* by the same method used to obtain s^* from the data. The Fourier transform was obtained and a spectral ratio calculated. While for the measured values of s^* the spectrum of one station was divided by that of another, to obtain d^* we divide each synthetic seismogram by the source wavelet spectra. The value d^* is then calculated by obtaining the best-fit linear gradient of $\ln A/A_0$ versus frequency in the frequency window 0.03–0.175 Hz. Taking the spectral ratio with the source spectrum means that d^* will equal zero when there has been no diffraction. It will be positive when there has been defocusing of the higher frequencies relative to the lower, and negative when there has been relative focusing. Note that the reason for the sign is that the gradient is multiplied by $-1/\pi$ to obtain d^*.

Diffraction of the wave energy around the plume results in a more complex pattern of d^* than caused by attenuation, as can be seen in Fig. 9. The wedge-shaped d^* variation beyond the plume is due to the development of a focal point and associated caustic. The frequency dependence of the focal-point position results in the maximum amplitude of higher and lower frequencies occurring at different distances beyond the plume centre, which is recorded in the value of d^*.

We first use Plume1 in the finite difference calculation and compare the resulting d^* variations with the observed s^*. Fig. 9(a) shows the calculated d^* variations as they would map on the Earth's surface; the scale in kilometres is shown along the horizontal axis. Iceland has a diameter of ~350 km. The two circles represent distances l and $2l$ from the centre of the plume, and the wave front propagates from the top of the diagram through the plume and towards the bottom, as indicated by the arrow. Diffraction around the plume results in three dominant stripes in the pattern of d^* parallel to the horizontal direction of ray propagation, with a negative band in the centre beyond the plume, flanked by higher-amplitude positive lobes. Plume1 produces only low-amplitude d^* variations which do not develop closer than ~300 km from the plume centre. Strong variations could thus not be observed on land in Iceland.

While Plume1 is not capable of producing d^* variations as close to Iceland as the variations in s^* observed, a model which is more highly diffracting could. The strength of the diffractor can be increased by increasing $\delta v_{\max}$ or decreasing l. While developing other models we initially chose to keep the integral of the velocity anomaly constant. Narrowing the plume (decreasing l) while increasing the velocity perturbation ($\delta v_{\max}$) results in the associated traveltime delays remaining nearly constant. Plume2 was derived from Plume1 in this way; Fig. 6 shows the velocity model. l has been reduced to 100 km and $\delta v_{\max}$ increased to −7.4 per cent. Fig. 9(b) shows d^* resulting from Plume2. The effect is to move the onset of the d^* variations closer to the centre of the plume, such that they can be observed at stations in Iceland.

Plume3 is derived from Plume2 by increasing the velocity perturbation further but without changing l. In developing this

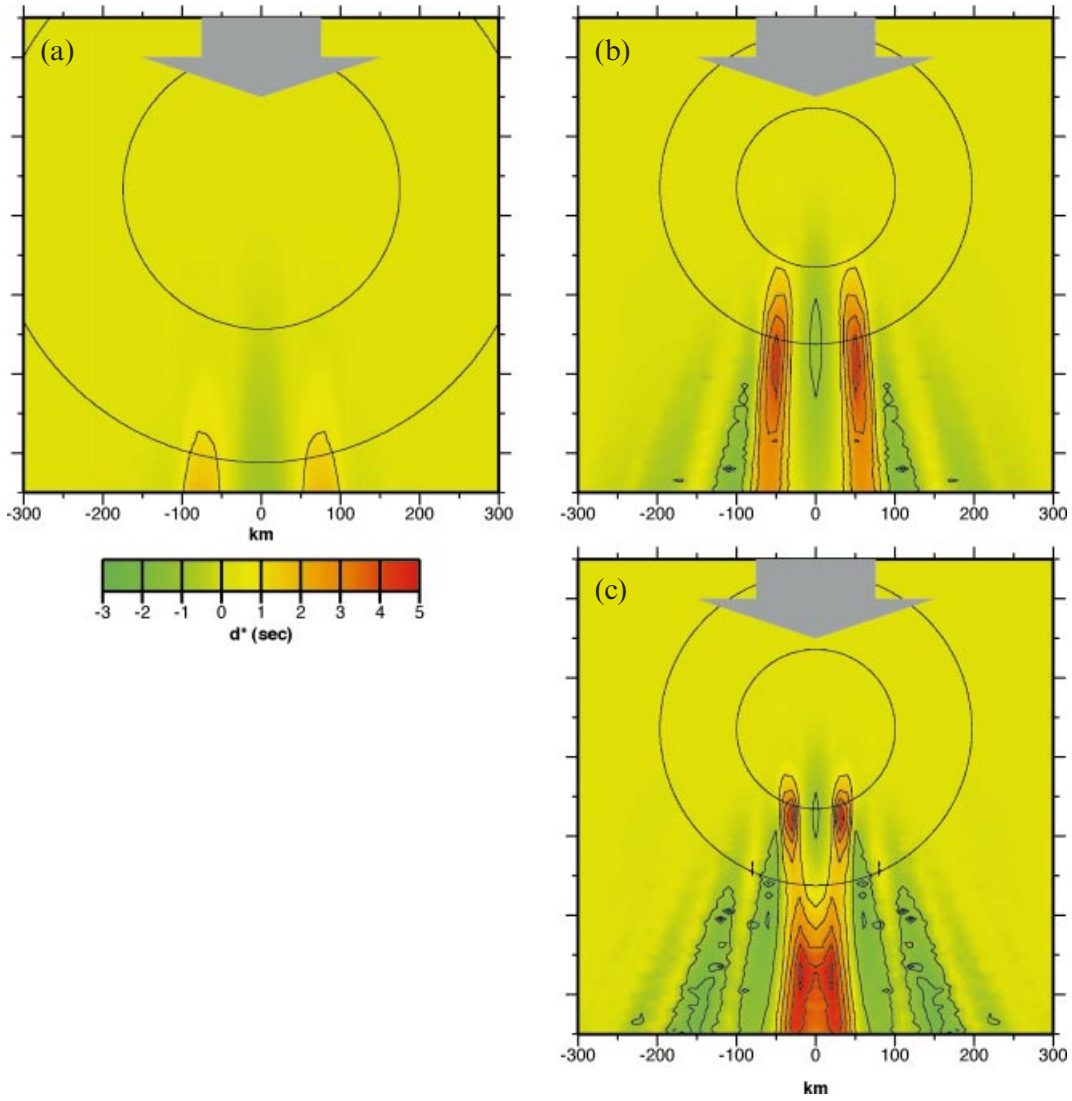

Figure 9. Apparent d^* variations due to diffraction for our three plume models. The plots are map view and show the d^* variations as they would be observed for shear-wave arrivals in Iceland; the horizontal and vertical scales are the same. Each plot shows an area of 600×600 km. Iceland is approximately 350 km in diameter. The circles represent distances of l and $2l$ from the centre of the plume. The horizontal component of the velocity for the rays in the model is shown by the arrow. d^* has been shaded and contoured. The contour interval is 1 s; zero is not contoured. (a) d^* variations for Plume1 ($dv_{max} = -4.2$ per cent and $l = 175$ km), the best-fit model to the structure of Wolfe *et al.* (1997). (b) d^* variations for Plume2 ($dv_{max} = -7.4$ per cent and $l = 100$ km). (c) d^* variations for Plume3 ($dv_{max} = -12$ per cent and $l = 100$ km), our best-fit model.

model we drop the constant traveltime constraint because we found it impossible to satisfy the data otherwise. Plume3 results in larger ray theoretical traveltimes than Plume1 or Plume2; the implications of this are discussed below. Fig. 6 shows the velocity model and Fig. 9(c) the apparent d^* variations. The effect of such a change is first to move the onset of the d^* anomaly closer to the centre of the plume and second to cause the positive lobes to merge.

5 OUR BEST-FIT MODEL

In our study we experimented with different plume models, calculated the d^* variations and compared them with s^* observed from the four events. We found that Plume3 provided the best qualitative fit between d^* and s^*. Figs 10(a)–(d) show d^* values calculated from Plume3 as colourscale. The arrow indicates the direction of wave-front propagation in the model. Overlain is a map of Iceland and the observed s^* values for the four events. The maps have been rotated so the backazimuths of each event are parallel to the direction of wave-front propagation in the model.

The correlation between d^* and s^* is good for Plume3. The model explains most of the s^* variations, unlike the t^* variations or d^* from Plume1 and Plume2. For each event we optimize the location of the centre of the plume by displacing it up to 60 km to obtain the best fit between s^* and d^*. These small variations would presumably be accounted for by slight asymmetries in the real plume. The wedge-shaped region of d^* values shows good agreement between d^* and s^*—the positive and negative values correlate, as do the locations of peak values.

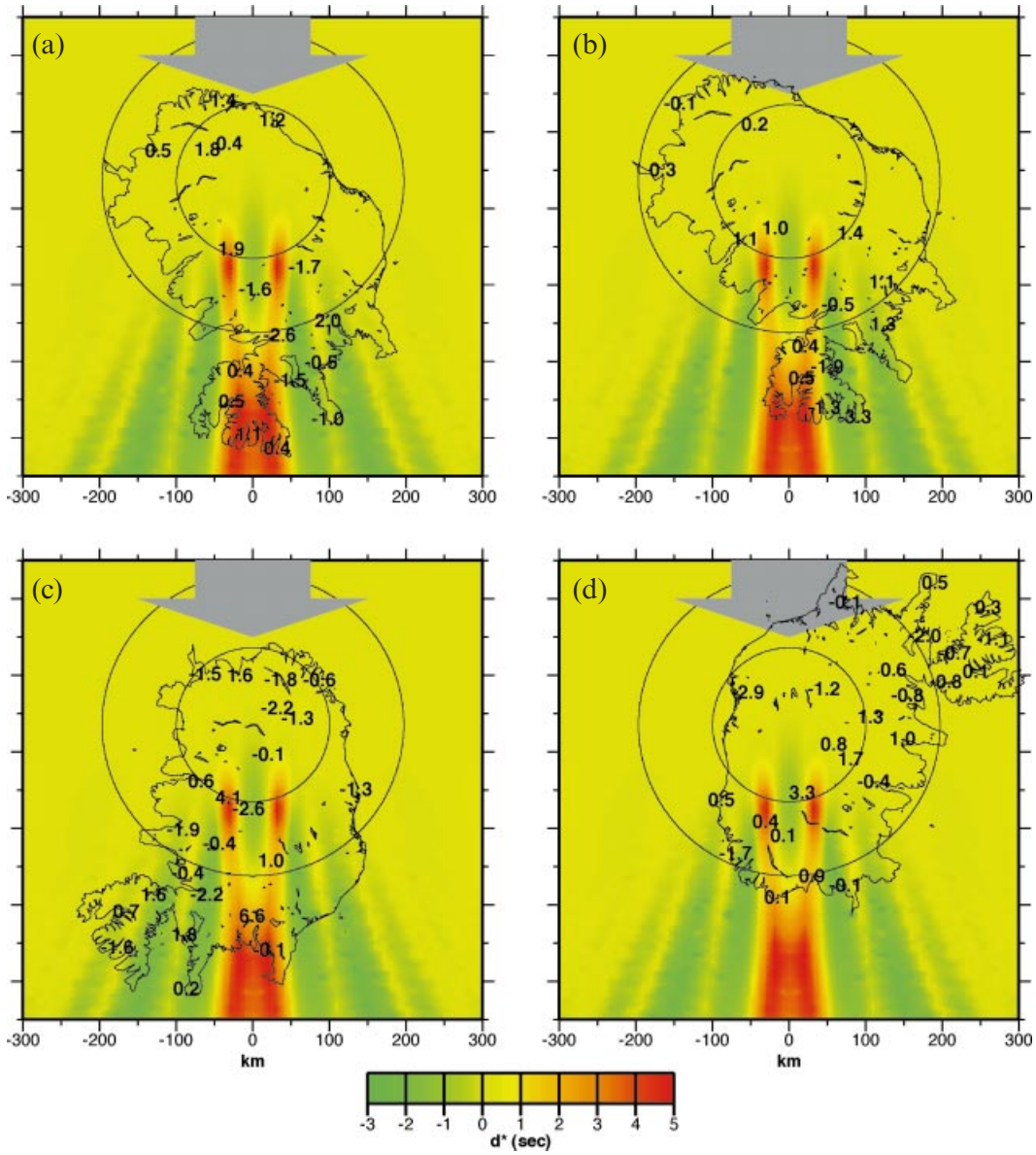

Figure 10. Comparison of the apparent d^* variation due to diffraction through our best-fit model (Plume3), with s^* observed for four teleseismic events. The colourscale shows the predicted d^* for rays traveling with a horizontal velocity component indicated by the arrow. The observations and the map of Iceland have been rotated such that the backazimuth for each event is parallel to the direction of ray propagation in the model. The circles indicate distances of l and $2l$ from the centre of the plume. The plots show good agreement in terms of the pattern of positive and negative values of d^* and s^*. (a) s^* for the Cyprus event of 1996 October 9. (b) s^* for the Aegean event of 1996 July 20. (c) s^* for the Kashmir event of 1996 November 19. (d) s^* for the Peru event of 1996 November 12.

It is difficult to quantify the goodness of fit of our modelling, since we primarily aimed for a qualitative agreement between the scatter shown in the observations of s^* and in the modelled d^*. Fig. 11 shows the statistical distribution of the s^* and d^* values obtained. Fig. 11(a) is a histogram of the d^* values calculated from Plume3. The histogram does not include d^* values between -0.1 and 0.1, of which there are several thousand corresponding to all the points not affected by the plume model. The distribution shows a steady increase in the number of d^* values from -3 to 0.5 s. There is a significant drop in the number of positive values, although the distribution extends to higher positive values than negative.

Fig. 11(b) shows the equivalent histogram for all s^* observations. It shows the same distribution. There is a gradual increase in the number of values from -3.5 to 2 s, then fewer but higher positive values. The s^* distribution is shifted relative to d^* as we impose the condition that the average value of s^* is zero: this is not the case for d^*. The s^* distribution is also a little broader than d^*, which we expect due to the effect of heterogeneity being excluded from our simplified plume model. Heterogeneity also explains variations in observations for rays that have not sampled the plume. The variations in Fig. 10(d) in the Westernfjord area (top right of the figure) range from -2.0 to 0.5 s, somewhat smaller than variations

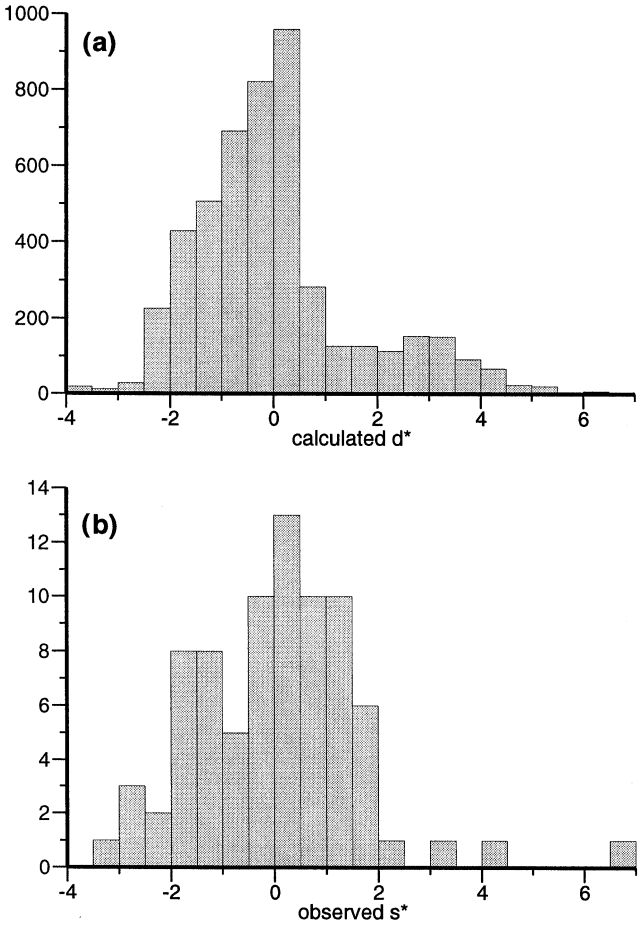

Figure 11. Histograms showing the distribution of d^* and s^* values. (a) Calculated d^* values for Plume3. The several thousand near-zero (between -0.1 and 0.1) d^* values have been removed from the distribution. They mainly represent rays which have not sampled the plume. (b) Observed s^* values for the four teleseismic events (Table 1).

observed in the wake of the plume, and less structured than the swaths of focused and defocused waves. Such variations could be modelled by introducing the effects of the plume head, which is missing from our cylindrical plume. Smaller heterogeneities beneath the stations may also have an effect. These variations could be included in a fully 3-D calculation, but only at great expense in terms of computer resources. Since this would also lead to a highly underdetermined problem, we did not attempt 3-D modelling.

Our starting model (Plume1) was a best-fit model to the velocity model of Wolfe *et al.* (1997) for the Iceland plume. However, it was not capable of producing the observed variations in d^*. Our best-fit model, Plume3, is both narrower and has a greater maximum velocity anomaly than Plume1; this is to be expected when we consider the methods of seismic tomography. Seismic tomography requires a degree of both damping and smoothing to prevent the propagation of errors. This results in velocity perturbations being reduced and the velocity structure being broadened. Wolfe *et al.* (1997) discuss resolution tests which indicate the plume can be no broader but do not discuss any tests suggesting its minimum width. If our model is a good representation of the Iceland plume, then the methods used by Wolfe *et al.* (1997) damped the maximum *S*-velocity anomaly from -12 per cent (Plume3) to -4.2 per cent. In addition, the plume radius, 100 km for Plume3, was broadened to 175 km. This suggests that the seismic tomography methods used by Wolfe *et al.* (1997) resulted in 65 per cent damping and 75 per cent broadening, which is within the resolution limits of their model (Wolfe, personal communication, 1997). These percentages do not take into account the effects of wave-front healing, however, which reduce the observed delay time and thus the magnitude of the velocity anomaly.

6 WAVE-FRONT HEALING

Our best-fit plume model, Plume3, has a significantly higher maximum velocity anomaly ($dv_{\max} = -12$ per cent) than tomographic estimates; for example, Wolfe *et al.* (1997) found a maximum *S*-velocity anomaly of -4.2 per cent (Plume1). Such a difference in velocity should be observed in traveltime delays in Iceland. *S*-wave arrival-time anomalies of ~ 7 s would be expected for Plume3, but only ~ 3 s for Plume1.

In the recent ICEMELT experiment on Iceland, Bjarnason *et al.* (1996) reported relative delay times for *P* and *S* waves greater than 1 and 3 s, respectively. In our preliminary study of the HOTSPOT data we find relative delay times of up to 3 and 6.5 s for *P* and *S* waves, respectively.

The difference between the calculated traveltime anomalies (ray theoretical) and those observed is explained by wave-front healing. We estimate the wave-front healing effect at the same frequency typically used to pick teleseismic *S*-wave arrivals on Iceland. We do this using our synthetic waveforms, which have a characteristic frequency of 0.07 Hz, calculated from the rise time.

To calculate the total reduction of the traveltime delay due to wave-front healing, we subtract the ray theoretical traveltimes in our model (without ray bending) from those calculated from the synthetic waveforms. We pick the times on the synthetic waveforms by finding the time at which the amplitude of the wavelet has risen to a specified amplitude. Fig. 12 shows the reduction in traveltime delay that would result for our three plume models. Plume1 (Fig. 12a) results in very little wave-front healing at distances that could be observed on land in Iceland (Iceland is ~ 350 km across). The delay time is reduced by 1 s due to healing for Plume2 (Fig. 12b). Plume3 (Fig. 12c) has a more significant effect, with a reduction in delay time of up to 3 s. These times can be considered as both the reduction in absolute traveltime due to healing and a reduction in relative delay times across Iceland as the healing only affects arrivals on the far side of the plume relative to the event.

We superimpose the velocity perturbation of Plume3 on IASP91 to calculate the maximum relative *S* delay time across Iceland of 7 s. Fig. 12 shows that wave-front healing could reduce that by as much as 3 s to a 4 s relative delay time, which is within the range observed. The size of these traveltime reductions due to wave-front healing makes it difficult to determine the true velocity anomaly for narrow plumes. An increase in the velocity anomaly may not be observed in terms of arrival time as the increased delay time is countered by a reduction in delay time due to wave-front healing.

7 DISCUSSION

We have shown that the pattern of s^* observations from shear-wave arrivals for four events at various azimuths can be

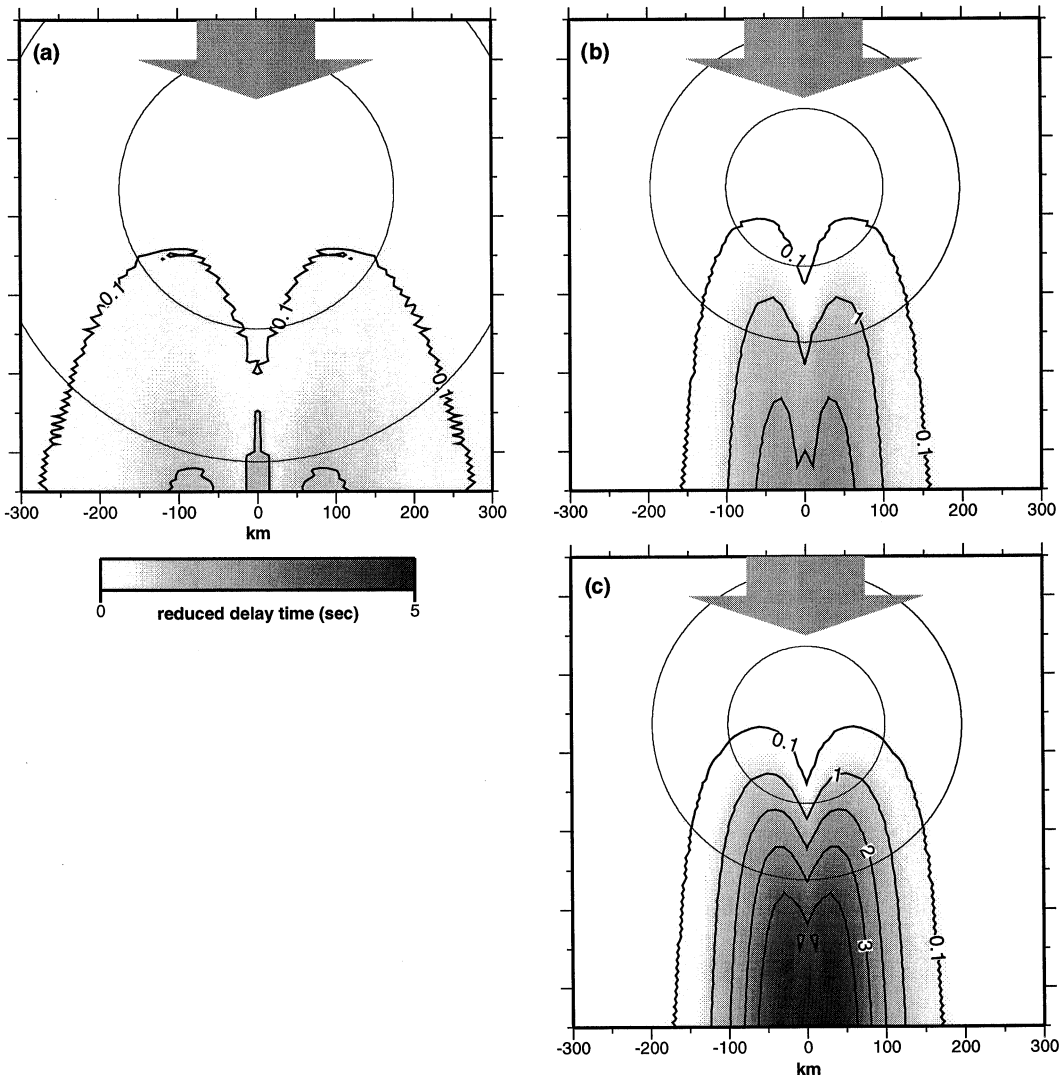

Figure 12. Reduced traveltime delay due to wave-front healing for our three plume models. The reduced traveltime is calculated by subtracting arrival time in the finite difference calculation from the ray theoretical arrival time. The horizontal component of the velocity for the rays in the model is indicated by the arrow. The circles indicate distances of l and $2l$ from the centre of the plume. The reduced delay time is contoured at 0.1, 1, 2, 3 s, etc. The healing only affects arrivals on the far side of the plume from the event. As a result it affects both the absolute delay and the relative delay across Iceland. (a) Reduced traveltime delay due to wave-front healing for Plume1, the best fit to the velocity model of Wolfe *et al.* (1997). There is little effect. (b) For Plume2 the effect is increased due to the reduced width of the plume—there is up to a 1 s reduction in traveltime delay. (c) For our best-fit model (Plume3) the reduced delay time can be as much as 3 s at distances observable in Iceland.

explained in terms of diffraction effects around a cylindrical plume model with $l = 100$ km and $\delta v_{\max} = -12$ per cent. Considerations of the anelastic attenuation (t^*) and diffraction (d^*) effects have been kept separate. The total observed variation is due to the sum of the two, eq. (5).

Combination of the two effects for our best-fit model, Plume3, is problematic as our finite difference calculation does not allow the correct computation of t^*. A ray theoretical estimate is inappropriate as empirical equations relating Q to velocity such as that used in Section 4.2 only hold for small velocity perturbations. We are still confident in our best-fit model, however, as the two effects, attenuation and diffraction, result in very different patterns of s^* variation. Diffraction results in alternating bands of positive and negative d^* values. Attenuation, however, results in a single maximum, grading from zero effect away from the plume to a positive maximum for a ray sampling most of the plume. The width of the t^* anomaly will also be broader than indicated in Fig. 7, and probably broader than Iceland even for the narrow plume we suggest. This is due to the Fresnel zone. The true width of the area sampled by the 'ray' is greater than one wavelength; that is, it is greater than 100 km for S waves. As a result, all rays arriving in Iceland will sample a large portion of the plume. The t^* effect will therefore be fairly constant across Iceland, and will be subtracted from our s^* values with the baseline shift.

Our estimates of plume width and velocity anomaly (Plume3) are significantly narrower and greater than previous, seismology-based estimates. Ray theoretical calculations suggest such a model produces larger traveltime variations than those observed. We find the effect of wave-front healing to be significant, however, reducing the observed relative delay

time by up to 40 per cent. This reduces the predicted relative delay times for Plume3 to within the range observed. This effect makes it impossible to observe large *S*-velocity anomalies in narrow plumes from traveltimes. An increased *S*-velocity anomaly is countered by the increased wave-front healing, resulting in little change in delay time.

While wave-front healing explains the difference between the velocity anomaly of Plume3 and previous, seismology-based estimates, it cannot explain the difference in plume width. We believe this to be due to the smoothing effects of tomographic methods. Our data favour a plume width l of the order of 100 km rather than the 175 km found by Wolfe *et al.* (1997).

Dynamical plume models based on surface observables in the North Atlantic provide another source of evidence for Icelandic plume structure. In such models the plume flux is well constrained; however, there is a trade-off between plume radius and maximum velocity anomaly, which is related to plume temperature. Ribe *et al.* (1995) compare a hot, narrow plume (temperature contrast $\sim$250 °C, radius $\sim$60 km) with a broader, cooler one (temperature contrast $<$100 °C, radius $>$300 km) . The broad plume model provides the best fit to observed depth anomalies along the Reykjanes Ridge, to the southwest of Iceland, but does not satisfy other observables, for example geochemistry and traveltime delays (Ito *et al.* 1996).

Ito *et al.* (1996) used a 3-D variable-viscosity dynamical plume beneath a diverging lithospheric lid. They too found that a broad, cool plume (temperature contrast 75 °C, radius 300 km) produced the best fit to observed crustal thickness and topographic and gravity anomalies. However, their narrow, hot plume (temperature contrast 170 °C, radius 60 km) matches the $^{87}Sr/^{86}Sr$ anomaly, which is considered to be the signature of primordial plume material. They also noted that the traveltime delays associated with the broad plume were less than half the magnitude of those observed. They concluded that the narrow plume is more appropriate for Iceland. Our model, with $l = 100$ km, falls between the 'broad' and 'narrow' plumes of Ito *et al.* (1996).

It is difficult to make a temperature estimate based on our -12 per cent *S*-velocity anomaly. We do not aim to do that here, but instead to illustrate that a -12 per cent *S*-velocity anomaly does not necessarily suggest temperatures outside the range of geochemically favoured estimates, which lie between 150 and 300 °C (e.g. McKenzie 1984; Sleep 1990; Shen *et al.* 1996). Simply using the laboratory measurements of Isaak (1992) on olivine we would obtain a δT of $\sim$1600 °C. This estimate does not include effects such as attenuation and partial melt fraction. The dispersive effects of attenuation could reduce δT by a factor of 2 to $\sim$800 °C (Karato 1993). In addition, the effects of small fractions of partial melt are significant and highly non-linear. A minute fraction of partial melt can easily result in a large drop in *S*-wave velocity if intergranular slip occurs. The aspect ratio of melt pockets is more important than the fraction of partial melt (Walsh 1969). Faul *et al.* (1994) estimate that the temperature could be reduced by an additional $\sim$400 °C per per cent melt. They also note that this number is highly dependent on the aspect ratio of the melt inclusions. When these effects are combined, our -12 per cent *S*-velocity anomaly becomes compatible with the geochemically favoured estimates of plume temperature. *S*-velocity anomalies in excess of 10 per cent have also been found by Van der Lee & Nolet (1997) in the upper mantle beneath the western US.

8 CONCLUSIONS

(1) We have successfully modelled the Icelandic plume as a cylindrical anomaly with a Gaussian-shaped velocity perturbation. The plume which fitted the frequency-dependent amplitude variations of *S*-wave arrivals across Iceland best had a maximum *S*-wave velocity perturbation of -12 per cent, falling to $1/e$ of that value at $l = 100$ km from the plume centre.

(2) This estimate of plume geometry is narrower, and it has a higher *S*-velocity anomaly than previous seismology-based estimates. This is because seismic tomography introduces broadening and dampening of the velocity model, whereas finite difference modelling of diffraction effects does not.

(3) The diffraction effects of the Iceland plume have a more significant effect on observed amplitude variations (as a function of frequency), i.e. t^*, than anelastic attenuation.

(4) In the case of the narrow plume that we have suggested here, wave-front healing can result in a reduction of observed relative delay times across Iceland of up to 40 per cent for teleseismic *S* waves at 0.07 Hz (the centre of the frequency band used for picking *S* arrivals). Wave-front healing counters any increased delay resulting from a greater velocity anomaly.

ACKNOWLEDGMENTS

This work was funded by NSF EAR/9417918 and NERC GST/02/1238. We would like to thank Tony Dahlen for regular discussions, Paul Friberg and Sid Hellman from the IRIS-PASSCAL project for their continuing support in the field and data handling operations, and all the Icelandic farmers who are lodging our instruments. The figures were produced with GMT (Wessel & Smith 1995).

REFERENCES

Aldridge, D.F., 1990. The Berlage wavelet, *Geophysics,* **55,** 1508–1511.

Bhattacharyya, J., Masters, G. & Shearer, P., 1996. Global lateral variations of shear wave attenuation in the upper mantle, *J. geophys. Res.,* **101,** 22 273–22 289.

Bjarnason, I.T., Wolfe, C.J., Solomon, S.C. & Gudmundson, G., 1996. Initial results from the ICEMELT experiment: body-wave delay times and shear-wave splitting across Iceland, *Geophys. Res. Lett.,* **23,** 459–462.

Courtney, R.C. & White, R.S., 1986. Anomalous heat flow and geoid across the Cape Verde Rise: evidence for dynamic support from a thermal plume in the mantle, *Geophys. J. R. astr. Soc.,* **87,** 815–867.

Davies, G.F., 1989. Mantle convection model with dynamic plate; topography, heat flow and gravity anomalies, *Geophys. J. R. astr. Soc.,* **98,** 461–464.

Faul, U.H., Toomey, D.R. & Waff, H.S., 1994. Intergranular basaltic melt is distributed in thin, elongated inclusions, *Geophys. Res. Lett.,* **21,** 29–32.

Halderman, T.P. & Davis, P.M., 1991. Qp beneath the Rio Grande and East African Rift zones, *J. geophys. Res.,* **96,** 10 113–10 128.

Houseman, G.A., 1990. The thermal structure of mantle plumes: axisymmetric or triple-junction?, *Geophys. J. Int.,* **102,** 15–24.

Isaak, D.G., 1992. High-temperature elasticity of iron-bearing olivines, *J. geophys. Res.,* **97,** 1871–1885.

Ito, G., Lin, J. & Gable, C.W., 1996. Dynamics of mantle flow and melting at a ridge-centered hotspot: Iceland and the Mid-Atlantic Ridge, *Earth planet. Sci. Lett.,* **144,** 53–74.

Karato, S., 1993. Importance of anelasticity in the interpretation of seismic tomography, *Geophys. Res. Lett.,* **20,** 1623–1626.

Lebedev, S. & Nolet, G., 1997. Waveform inversions: attenuation vs scattering, *EOS, Trans. Am. geophys. Un.,* **78,** Suppl., S216.

Lees, J.M. & Lindley, G.T., 1994. Three-dimensional attenuation tomography at Loma Prieta: inversion of t* for Q, *J. geophys. Res.,* **99,** 6843–6863.

Loper, D.E. & Stacey, F.D., 1983. The dynamic and thermal structure of deep mantle plumes, *Earth planet. Sci. Lett.,* **33,** 304–317.

Marquering, H., 1991. A finite-difference simulation of acoustic waves, *MSc thesis,* Utrecht University, the Netherlands.

McKenzie, D., 1984. The generation and compaction of partially molten rock, *J. Petrol.,* **25,** 713–765.

McKenzie, D., Roberts, J.M. & Weiss, N.O., 1974. Convection in the Earth's mantle: towards a numerical simulation, *J. Fluid Mech.,* **62,** 465–538.

Morgan, W.J., 1971. Convection plumes in the lower mantle, *Nature,* **230,** 42–43.

Nataf, H.C. & Ricard, Y., 1996. 3SMAC: An a priori tomographic model of the upper mantle based on geophysical modeling, *Phys. Earth planet. Inter.,* **73,** 101–122.

Olsen, P., 1990. Hot spots, swells and mantle plumes, in *Magma Transport and Storage,* pp. 33–51, ed. Ryan, M.P., John Wiley, Chichester.

Ribe, N.M., Christensen, U.R. & Theibing, J., 1995. The dynamics of plume-ridge interaction, 1: ridge-centered plumes, *Earth planet. Sci. Lett.,* **134,** 155–168.

Shen, Y., Solomon, S.C., Bjarnason, I.T. & Purdy, G.M., 1996. Hot mantle transition zone beneath Iceland and the adjacent Mid-Atlantic Ridge inferred from P-to-S conversions at the 410 and 660 discontinuities, *Geophys. Res. Lett.,* **23,** 3527–3530.

Slack, P.D., Davis, P.M., Baldridge, W.S., Olsen, K.H., Glahn, A., Achauer, U. & Spence, W., 1996. The upper mantle structure of the Rio Grande rift region from teleseismic P and S wave travel time delays and attenuation, *J. geophys. Res.,* **101,** 16 003–16 023.

Sleep, N.H., 1990. Hotspots and mantle plumes: some phenomenology, *J. geophys. Res.,* **95,** 6715–6736.

Taylor, S.R., Bonner, B.P. & Zandt, G., 1986. Attenuation and scattering of broadband P and S waves across north America, *J. geophys. Res.,* **91,** 7309–7325.

Tilmann, F.J., McKenzie, D. & Priestley, K.F., 1998. P and S wave scattering from mantle plumes, *J. geophys. Res.,* **103,** 21 145–21 163.

Tryggvasson, K., Husebye, E.S. & Stefansson, R., 1983. Seismic image of the hypothesized Icelandic hot spot, *Tectonophysics,* **100,** 97–118.

Van Decar, J.C. & Crosson, R.S., 1990. Determination of teleseismic relative phase arrivals using multi-channel cross-correlation and least squares, *Bull. seism. Soc. Am.,* **80,** 150–169.

Van der Lee, S. & Nolet, G., 1997. Upper mantle *S*-velocity structure of North America, *J. geophys. Res.,* **102,** 22 815–22 838.

Walsh, J.B., 1969. New analysis of attenuation in partially melted rock, *J. geophys. Res.,* **74,** 4333–4337.

Watson, S. & McKenzie, D., 1991. Melt generation by plumes: a study of Hawaiian volcanism, *J. Petrol.,* **32,** 501–537.

Wessel, P. & Smith, W.H.F., 1995. New version of the Generic Mapping Tools released, *EOS, Trans. Am. geophys. Un.,* **76,** Suppl., 329.

Wilson, J.T., 1963. A possible origin of the Hawaiian islands, *Can. J. Phys.,* **41,** 863.

Wolfe, C.J., Bjarnason, I.T., VanDecar, J.C. & Solomon, S.C., 1997. Seismic structure of the Iceland mantle plume, *Nature,* **385,** 245–247.

Wu, H. & Lees, J.M., 1996. Attenuation structure of Coso geothermal area, California, from wave pulse widths, *Bull. seism. Soc. Am.,* **86,** 1574–1590.